



UvA-DARE (Digital Academic Repository)

A spectral-timing approach to the study of AGN outflows

de Jesus Silva, C.V.

Publication date

2018

Document Version

Other version

License

Other

[Link to publication](#)

Citation for published version (APA):

de Jesus Silva, C. V. (2018). *A spectral-timing approach to the study of AGN outflows*. [Thesis, fully internal, Universiteit van Amsterdam].

General rights

It is not permitted to download or to forward/distribute the text or part of it without the consent of the author(s) and/or copyright holder(s), other than for strictly personal, individual use, unless the work is under an open content license (like Creative Commons).

Disclaimer/Complaints regulations

If you believe that digital publication of certain material infringes any of your rights or (privacy) interests, please let the Library know, stating your reasons. In case of a legitimate complaint, the Library will make the material inaccessible and/or remove it from the website. Please Ask the Library: <https://uba.uva.nl/en/contact>, or a letter to: Library of the University of Amsterdam, Secretariat, Singel 425, 1012 WP Amsterdam, The Netherlands. You will be contacted as soon as possible.

The variability of the warm absorber in I Zwicky 1 as seen by XMM-Newton

C.V. Silva, E. Costantini, M. Giustini, G. A. Kriss, W. N. Brandt, L. C. Gallo, and D. R. Wilkins

Submitted to Monthly Notices of the Royal Astronomical Society (MNRAS)

Abstract

We present new XMM-Newton observations of the warm absorber in I Zwicky 1, taken simultaneously with HST-COS observations. This luminous and nearby narrow-line Seyfert 1 galaxy shows ionized absorption by two components of outflowing gas; a low and a high-ionization phase with $\log \xi \sim 0$ and $\log \xi \sim 2$ respectively. Detailed modeling of these data reveal a complex and variable multi-phase warm absorber. However, we find the changes in the ionization state of the gas not to be correlated with the variability of the intrinsic source, in apparent contrast with photoionization equilibrium. Such puzzling behaviour cannot be understood under classical warm absorber geometries. This variability instead hints at a close connection between the two gas components, possibly both directly connected to the accretion disc activity. We thus suggest a phenomenological model capable of explaining these observations, consisting of a clumpy outflow where the high and the low-ionization components are closely linked. Changes in ionization over the years are mainly driven by the different densities of the clumps crossing the observer's line-of-sight, in which the 'skin' layer facing the source accounts for the more ionized component.

4.1 Introduction

Ionized outflows in Active Galactic Nuclei (AGN) have long been a subject of study in the X-ray and ultraviolet (UV) domains. Such gas is frequently referred to as a warm absorber (WA) and its presence is inferred from the detection of blueshifted absorption lines in the high-resolution spectra of these sources (for a review see Crenshaw et al. 2003a). It has been estimated that roughly 60% of Seyfert 1 galaxies show the presence of a warm absorber in their spectra (e.g. Crenshaw et al. 1999; Laha et al. 2014).

Despite extensive studies, the origin and physical structure of warm absorbers is not yet fully understood. In the UV, the observed transitions belong solely to a few important ions (e.g. C IV, N V, O VI, and Lyman- α) but due to the high spectral resolution available in this band several velocity components can be distinguished, while in the X-rays dozens of blurred transitions make it possible to estimate the ionization state and column density of the different gas components. Other important characteristics such as the spatial extent of the absorbing gas and its distance relative to the central source are harder to determine. The spatial location of the outflows in particular yields valuable information for AGN feedback studies (e.g. Di Matteo et al. 2005; Hardcastle et al. 2007; Crenshaw & Kraemer 2012; Fabian 2012). An estimate of the density n of the gas grants an estimate of its distance r to the central source since the ionization parameter ξ is a function of both these properties, as well as of the ionizing luminosity L_{ion} , $\xi = L_{\text{ion}}/nr^2$. In the UV, sensitive absorption lines from meta-stable transitions can be used to measure the density of the gas (e.g. Kraemer et al. 2006; Arav et al. 2008, 2015). In the X-rays, the density can be estimated through variability studies. The intrinsic X-ray source is variable and changes in the ionizing flux induce a response in the ionization state of the gas, characterized by an equilibrium timescale. The time it takes for the gas to reach equilibrium with the ionizing continuum is dependent on the properties of the gas, specifically on its density (Nicastrò et al. 1999; Krolik & Kriss 2001; Silva et al. 2016). Obtaining the density, and subsequently the distance, of the warm absorber via this method requires detailed monitoring of the source and has been applied for several objects through time-resolved spectroscopy (e.g. Krongold et al. 2007; Steenbrugge et al. 2009) and time-dependent photoionization studies (Nicastrò et al. 1999; Kaastra et al. 2012). However, some sources appear to show an even more complex behaviour. For example, in MR 2251-178 there seems to be no connection between the ionization parameter and the X-ray luminosity (Kaspi et al. 2004). More recently, Longinotti et al. (2013) reported the discovery of intrinsic ionized absorption in Mrk 335, for which no correlation was found between the warm absorber variability and the X-ray flux.

Multiwavelength UV-X-ray campaigns are key to characterize the outflow (for a review see Costantini 2010). Previous studies have suggested ionized absorption in

the X-rays to be a manifestation of the same gas that absorbs in the UV (see e.g. Kaspi et al. 2002; Arav et al. 2007; Ebrero et al. 2011). Unveiling this connection between the UV and X-ray absorbing gas is fundamental to understanding the nature of warm absorbers and, consequently, assess the impact of the gas on the surrounding environment.

I Zwicky 1 (I ZW 1) is a narrow-line Seyfert 1 galaxy located at a redshift of $z=0.061169$ (Springob et al. 2005). Previous XMM-Newton observations of this source revealed absorption by two components of ionized gas and an apparent anti-correlation between X-ray ionization and ionizing luminosity on timescales of years (Costantini et al. 2007a). In this work, we further analyse the absorption-line rich soft X-ray spectrum of I ZW 1 as recently observed by XMM-Newton during a multiwavelength campaign, also including simultaneous observations with HST (PI: Costantini, E.). The analysis of the HST data will be published in a subsequent paper (Giustini et al. in prep.).

Details on these observations and data reduction are reported in section 4.2. Section 4.3 refers to the detailed analysis of the data and modelling of the spectral features through time-averaged spectral fitting, flux-resolved spectroscopy and time-resolved spectroscopy. Section 4.4 is devoted to an extensive discussion of our results and possible physical scenarios for the nature of the warm absorber. The conclusions and a summary of our work can be found in section 4.5.

We use a flat cosmological model with $\Omega_m = 0.3$, $\Omega_\Lambda = 0.7$, and $\Omega_r = 0.0$, together with a Hubble constant $H_0 = 70 \text{ km s}^{-1} \text{ Mpc}^{-1}$. For the spectral modelling in this paper we have assumed solar abundances (Lodders et al. 2009) and a Galactic column density of $N_{\text{Htot}} = 6.01 \times 10^{20} \text{ cm}^{-2}$, which includes both the atomic and molecular hydrogen components (Elvis et al. 1989; Willingale et al. 2013). The errors quoted in this paper are 1σ errors unless otherwise stated.

4.2 Observations and data reduction

I ZW 1 was observed by XMM-Newton during two consecutive orbits on January 21 and January 22, 2015 (hereafter observations 301 and 801, respectively). For these observations, the RGS instrument (den Herder et al. 2001) was operated in multipointing mode. Point source photons of a given energy are always recorded in the same pixel of the detector due to the pointing stability of XMM-Newton. This means that if bad pixels in the detectors coincide with spectral features of interest, these may be lost. Multipointing mode uses five different pointings with offsets in the dispersion direction. In this way, the bad pixels, which often hamper the analysis of narrow spectral features, fall at a different energies for each pointing. Combining the spectra allows us to recover the true spectrum, at the expense of a slightly lower signal to noise ratio at the position of the bad pixel.

In the analysis, we took care of manually selecting the stable orbit portion for each of the pointings. This step is not currently handled automatically by the SAS pipeline. In practice, an additional good-time-interval table was used, in addition to the background event-filter, to select the events belonging to the stable part of the orbit. This led to a loss of only ~ 1 ks of effective exposure time per orbit. Furthermore, observation 801 was affected by episodes of background flaring. We selected only the background events with count rate less than 0.2 cts s^{-1} , as recommended by the SAS guidelines. The background filtering led to a loss of about 21 ks. The total net exposure time (including both orbits) is then 258 ks with 123497 ± 388 net source counts.

4.3 Spectral analysis

The absorption-line rich soft X-ray spectra obtained from RGS during the two observations were analysed using the fitting package SPEX v.3.02 (Kaastra et al. 1996). SPEX photoionization absorption model is able to model the complex absorption features observed in the spectra taking into account all relevant ions in a consistent manner. The XABS model calculates the transmission of a slab of material in photoionization equilibrium, by interpolating over a fine grid of column density N_{H} and ionization values $\log \xi$. The ionization balance is given as an input to XABS and is calculated with CLOUDY v.13.01 (Ferland et al. 2013) using the spectral energy distribution (SED) specific for these observations, for which the ionizing luminosity is calculated between 1 - 1000 Ryd.

The SED was constructed by using the simultaneous observations of I ZW 1 in 2015, taken with XMM-Newton and HST. The shape of the broad X-ray ionizing continuum (0.5 - 10 keV) is obtained by fitting the time-averaged spectrum of the EPIC-pn camera on board XMM-Newton. This phenomenological fit consists of a broken-power law with $\Gamma_1 \sim 3.02$, $\Gamma_2 \sim 2.26$, and an energy spectral break at $\sim 1.4 \text{ keV}$. The unabsorbed (both of Galactic and local ionized absorption) continuum is then used to construct the SED. The UV data refer to simultaneous observations with the COS instrument on HST, while the XMM optical monitor (OM) extends the data to the optical band. Both the COS and OM data were corrected for the effects of interstellar extinction. At longer wavelengths the SED was completed by making use of the default AGN continuum in CLOUDY (Mathews & Ferland 1987). The continuum was extended above 10 keV, with a cutoff at $\sim 150 \text{ keV}$. The broadband SED is presented in Fig. 4.1.

The RGS energy range is limited, and thus we opted to fit a phenomenological continuum model that describes the data well in this range. The continuum shape for each observation was best described by a broken power-law (see Table 4.1). We

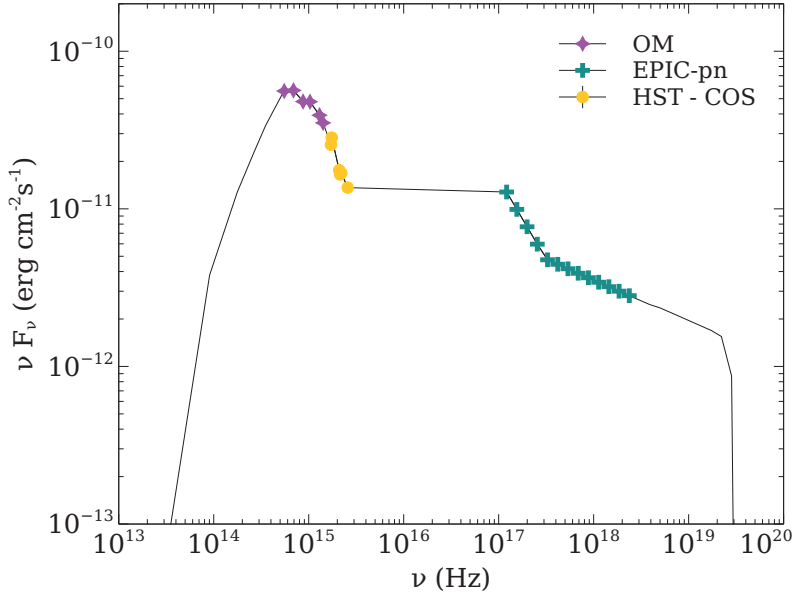


Figure 4.1: Adopted spectral energy distribution of IZW 1 based on the time-averaged simultaneous observations from XMM-Newton and HST in 2015.

have then combined the two observations in sectors¹. In this way we are able to fit the spectra of the two observations simultaneously, increasing the signal to noise ratio to constrain the warm absorber parameters, but still allowing continuum spectral changes between observations. Throughout the analysis, we use the C-statistic as shown in Kaastra (2017b), and the optimal data bin size, which rebins the data taking into account the signal to noise ratio as well as the instrumental resolution (see Kaastra & Bleeker 2016, for details). The optimal bin size can be achieved with the command `OBIN` in `SPEX`.

The residuals left from fitting the continuum ($C\text{-stat}/d.o.f. \sim 4737/3723$) clearly indicate absorption features, which were already identified in the past as two distinct warm absorber components (Costantini et al. 2007a). Adding a photoionization absorption model to the fit resulted in an improvement for which we reached $C\text{-stat}/d.o.f. \sim 4612/3719$. This model accounts for strong absorption features observable around 21 - 25 , due to multiple oxygen transitions (O V - O VII), as well as for the iron unresolved transition array (UTA). Finally, an additional photoionization absorption model is required to fit residuals at shorter wavelengths (10 - 17) such as the O VIII edge and the Fe L complex, which results in $C\text{-stat}/d.o.f. \sim 4565/3715$. Our best-fit model to the combined RGS spectra thus confirms the presence of two distinct

¹More information on how to create different sectors to analyse several observations simultaneously in `SPEX` can be found at <http://var.sron.nl/SPEX-doc/cookbookv3.0/cookbook.html>

Table 4.1: Best-fit parameters for the underlying continuum of the RGS spectra. Fluxes are in units of 10^{-12} erg s $^{-1}$ cm $^{-2}$, unabsorbed luminosities in units of 10^{43} erg s $^{-1}$.

Param.	Obs. 301	Obs. 801
Γ_1	2.93 ± 0.01	2.98 ± 0.01
Γ_2	2.52 ± 0.1	2.47 ± 0.1
$E_{\text{break}}(\text{keV})$	1.4 ± 0.1	1.4 ± 0.1
$F_{0.5-2 \text{ keV}}$	6.64 ± 0.07	7.39 ± 0.09
$L_{0.5-2 \text{ keV}}$	8.54 ± 0.09	9.5 ± 0.1

Table 4.2: Best-fit parameters for the combined fit of the 2015 observations. Components 1 and 2 correspond to the low and high-ionization phases, respectively.

	N_{H} ($\times 10^{20} \text{cm}^{-2}$)	$\log \xi$	Velocity (km s $^{-1}$)	σ_{rms} (km s $^{-1}$)
Comp 1	3.4 ± 0.4	-0.23 ± 0.06	-1870 ± 70	70 ± 10
Comp 2	9 ± 2	1.96 ± 0.05	-2500 ± 100	30 ± 10

photoionized components, a low and a high-ionization phase, see Fig. 4.2. Component 1, the low-ionization phase ($\log \xi \sim -0.2$) has a column density $N_{\text{H}} \sim 3.4 \times 10^{20} \text{cm}^{-2}$ and an outflow velocity $v_{\text{out}} \sim 1900 \text{ km s}^{-1}$. The high-ionization phase ($\log \xi \sim 2$, hereafter component 2) has a column density $N_{\text{H}} \sim 9 \times 10^{20} \text{cm}^{-2}$ and an outflow velocity $v_{\text{out}} \sim 2500 \text{ km s}^{-1}$. The root mean square width of the absorption lines was constrained by our fit to be $\sigma_{\text{rms}} \sim 70 \text{ km s}^{-1}$ for component 1 and $\sigma_{\text{rms}} \sim 30 \text{ km s}^{-1}$ for component 2. The best-fit parameters for the continuum are presented in Table 4.1 and the best-fit parameters for the warm absorber components are presented in Table 4.2. While fitting the spectrum only these four parameters for each XABS model were free to vary. We fixed the line-of-sight covering factor of the gas to unity. Looking at the residuals, there could be some off-set from the best-fit model, particularly at low energies. This would likely be due to the complexity of the of the continuum which in our model is represented in a simplified manner. Our analysis did not reveal the presence of additional absorber components.

4.3.1 Flux-resolved spectroscopy

To investigate if there are any changes to the absorber parameters when considering different source flux levels, we have divided the data according to their flux and analysed the averaged high and medium/low flux spectra separately. Based on the time variability of the source and corresponding flux levels, we have selected time intervals corresponding to periods of high and medium/low flux throughout the observations. The criteria for the selection took as a basis the broad-band light curves (0.3-10.0 keV), for which we determined the cut rate to be approximately at 10 cts/s

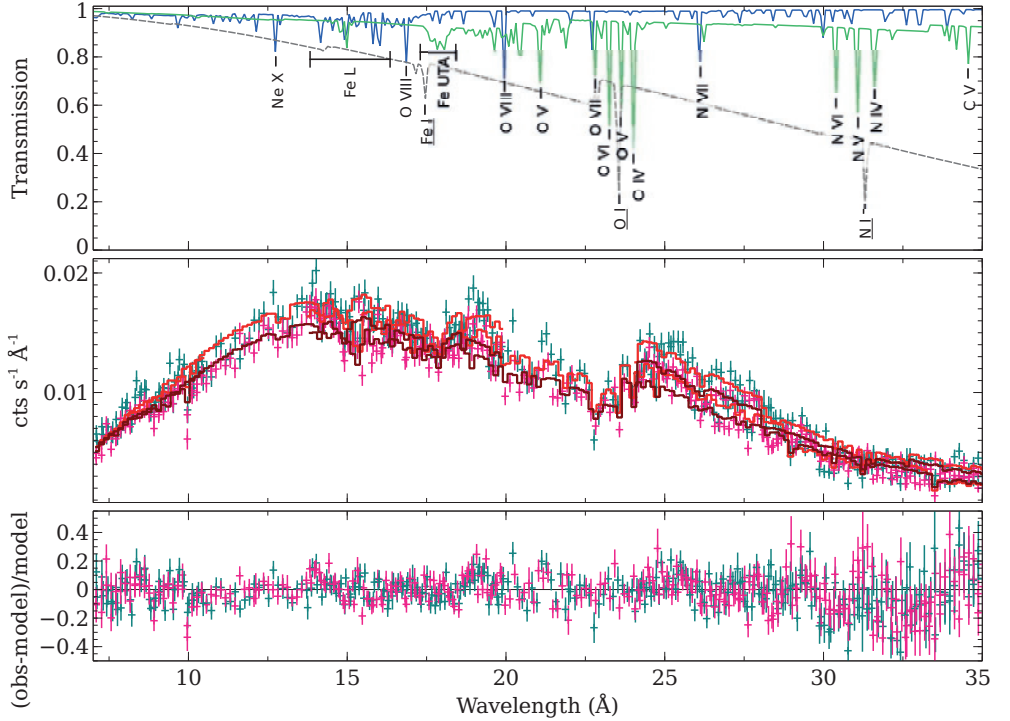


Figure 4.2: Best-fit parameters for the combined fit of the 2015 observations. The upper panel shows the transmission spectra of the two warm absorber models. The low-ionization component (component 1) is shown in green and the high-ionization component (component 2) is shown in blue. The strongest absorption features are labelled. The grey dashed-line refers to Galactic absorption and the features it produces are underlined. The middle panel shows the data (magenta, green) and the best-fit model (dark red, red) for observations 301 and 801 respectively. Data from both RGS instruments are presented. The lower panel shows the respective residuals.

(see Fig. 4.3). This cut rate ensures that there will be good signal-to-noise ratio for the medium/low flux spectrum while the flare observed in the last observation mostly dominates the high-flux state. We have then created two RGS spectra according to this flux selection and fitted the resulting averaged medium/low and high-flux spectra. The medium/low spectrum has an average count rate of $\sim 0.49 \pm 0.01$ cts/s and the high-flux spectrum has an average count rate of $\sim 0.68 \pm 0.01$ cts/s. Taking advantage of the constraints we obtained by fitting the two observations simultaneously, we now fit the different flux levels in a similar fashion. We start by fixing the warm absorber parameters to the best-fit parameters obtained previously (see Table 4.2) and allowed the continuum to adjust, since both the normalization and spectral shape could vary. We have then allowed the warm absorber parameters in the XABS models

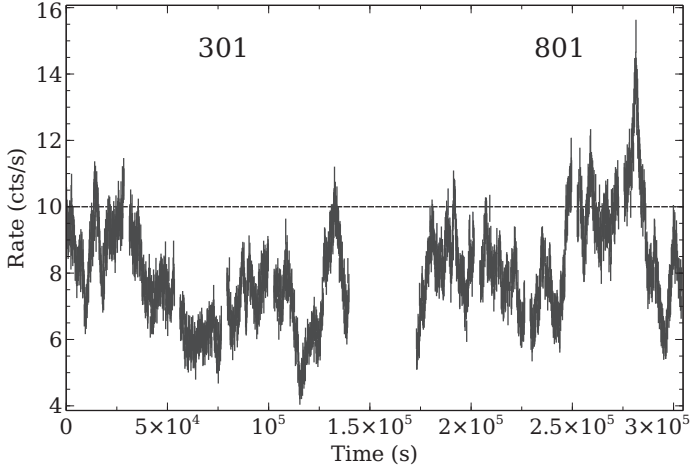


Figure 4.3: I ZW 1 broad-band light curves (0.3 - 10.0 keV) extracted from the EPIC-pn observations. The dashed line marks the cut rate for the selection of the medium/low and high-flux levels.

Table 4.3: Best-fit parameters for the underlying continuum of medium/low and high RGS spectra. Fluxes are in units of 10^{-12} erg s $^{-1}$ cm $^{-2}$, unabsorbed luminosities in units of 10^{43} erg s $^{-1}$.

Param.	high-flux	medium/low flux
Γ_1	2.92 ± 0.03	2.97 ± 0.02
Γ_2	2.2 ± 0.2	2.5 ± 0.2
$E_{\text{break}}(\text{keV})$	1.3 ± 0.1	1.3 ± 0.1
$F_{0.5-2 \text{ keV}}$	9.8 ± 0.1	6.7 ± 0.1
$L_{0.5-2 \text{ keV}}$	12.7 ± 0.2	8.6 ± 0.1

to vary, with the exception of the widths of the lines, σ_{rms} , that were fixed to the values of Table 4.2.

The spectral continuum shape is similar at low energies ($\Gamma_1 = 2.92 \pm 0.03$ for the high-flux spectrum and $\Gamma_1 = 2.97 \pm 0.02$ for the low-flux spectrum), and both break around 1.3 keV. At higher energies, $\Gamma_2 = 2.2 \pm 0.2$ and $\Gamma_2 = 2.5 \pm 0.2$ for the high-flux and low-flux spectra respectively. The best-fit parameters for the continuum are presented in Table 4.3. In terms of the behaviour of the warm absorber, the spectral fit does not reveal significant differences between the flux states. Fig. 4.4 shows the results of the modelling of the high and medium/low-flux spectra. For the high-flux spectrum, our best-fit model corresponds to $C\text{-stat}/d.o.f. \sim 2579/2311$. The best-fit to the medium/low flux spectrum corresponds to $C\text{-stat}/d.o.f. \sim 2849/2412$. The residuals are consistent with the residuals left by our best-fit model for the two observations combined.

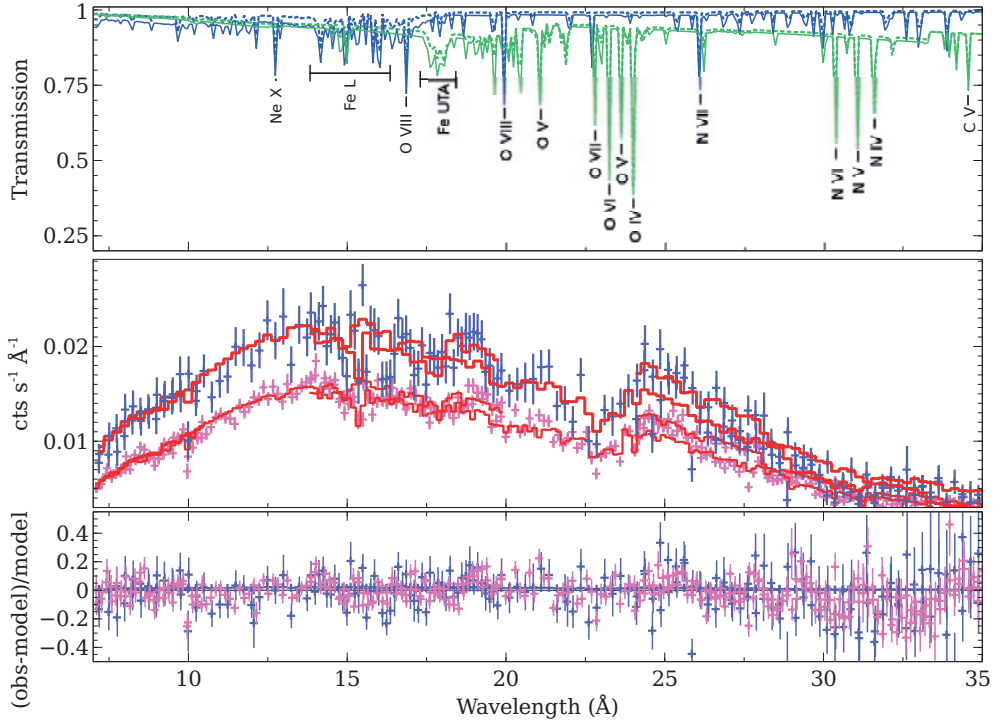


Figure 4.4: Best-fit parameters for the high and medium/low spectra. The upper panel shows the transmission spectra of the two warm absorber models. The high-flux transmission spectrum is shown by the dashed lines, while the medium/low flux transmission spectrum is shown by the solid lines. As previously, the low-ionization component (component 1) is shown in green and the high-ionization component (component 2) is shown in blue. The middle panel shows the high-flux spectrum (purple) and the medium/low flux spectrum (magenta). The best-fit model for each spectrum is represented by the red solid lines. The bottom panel shows the respective residuals.

Table 4.4: Best-fit parameters for the medium/low and high-flux spectra.

		N_{H} ($\times 10^{20} \text{cm}^{-2}$)	$\log \xi$	Velocity (kms^{-1})
Comp 1	low-flux	3.3 ± 0.5	-0.3 ± 0.1	-1870 ± 80
	high-flux	4.3 ± 0.5	0.0 ± 0.1	-1900 ± 200
Comp 2	low-flux	7 ± 3	2.0 ± 0.1	-2500 ± 200
	high-flux	15 ± 6	2.0 ± 0.1	-2500 ± 400

The most interesting variation is the behaviour of the column density of the most ionized component, component 2. Our fit suggests that column density of this gas phase during the high-flux state could be higher than during the medium/low flux periods (see Table 4.4). As can be seen from the transmission spectrum in Fig. 4.4, this difference is noticeable in the Fe-L complex which is highly sensitive to luminosity variations (Behar et al. 2001). The low-ionization component, component 1, seems to be immune to different flux levels (see Table 4.4). Despite the flux levels being very different, especially during the flare, in which the flux increases by approximately a factor of two, we do not observe a significant change in ionization.

4.3.2 Time-resolved spectroscopy

We investigate in more depth behaviour of the warm absorber, particularly how its ionization and column density behave as the flux changes in time. For this, we use time resolved spectroscopy to investigate how the warm absorber behaves on shorter timescales.

Long-time segments

We have considered at first two time segments per each orbit. The first segment of observation 301 is the combination of the first two pointings, while the second segment is the combination of the remaining three pointings. As for observation 801, the first 3 pointings were combined to create the first segment, and the remaining two pointings constitute the second segment (see top panel of Fig. 4.5). We probe here timescales of ~ 50 -80 ks. Combining individual pointings ensures both the elimination of bad pixels and a fair signal-to-noise ratio. The rationale behind this combination in particular relies on an attempt to combine, and analyse, similar flux levels, while ensuring a high signal-to-noise ratio. To fit the spectra we used a similar procedure to the one implemented in the flux resolved analysis. We started by using the best-fit model to the combined fit of the 2015 observations, and fixing the warm absorber parameters. We first fitted for the continuum by allowing the normalization of the power-law, the power-law indexes and the spectral break energy to vary. Subsequently we fitted the warm absorber parameters of components 1 and 2, leaving the column density and ionization of the gas as free parameters, while the continuum parameters remained thawed. The outflow velocity was kept fixed during the fits as well as the width of the absorption lines to the values from Table 4.1. The best-fit parameters are listed in Table 4.5.

Regarding the ionization state of the gas, both components do not seem to vary within the errors (see middle panel on Fig. 4.5). Thus, it is not possible to assess whether the gas is in equilibrium with the ionizing continuum for the considered timescales or if it is able to respond to the flux variations during these observations,

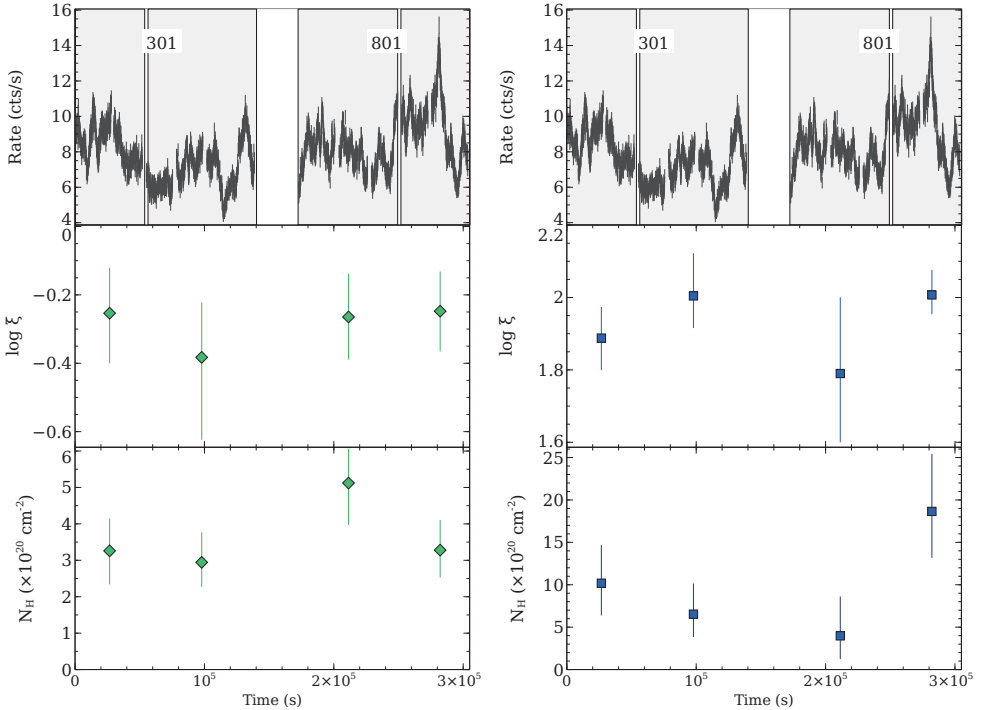


Figure 4.5: Best-fit parameters for the long time segments. This plot shows the behaviour of $\log \xi$ (middle panel) and N_{H} (bottom panel), for each of the long time segments selected (top panel).

Table 4.5: Best-fit parameters of the long time segments. The count rate refers to the RGS spectra.

	N_{H_1} (10^{20} cm^{-2})	N_{H_2} (10^{20} cm^{-2})	$\log \xi_1$	$\log \xi_2$	Rate (cts/s)	C-stat/ <i>d.o.f.</i>
1	3 ± 1	10 ± 4	-0.3 ± 0.1	1.9 ± 0.1	0.518 ± 0.002	2612/2272
2	3 ± 1	7 ± 3	-0.4 ± 0.2	2.0 ± 0.1	0.444 ± 0.003	4104/3458
3	5 ± 1	4 ± 4	-0.3 ± 0.1	1.8 ± 0.2	0.476 ± 0.002	3046/2275
4	3 ± 1	19 ± 6	-0.2 ± 0.1	2.00 ± 0.06	0.584 ± 0.004	2484/2325

since such changes would not be possible to be detected with the present statistics. Variability in the column density of the warm absorber components is formally not detected at these timescales, although component 2 appears to increase in column density during the second observation (see lower panel of Fig. 4.5). Motivated by these results, we attempted to fit the individual pointings separately and investigate further possible column density variations on shorter timescales.

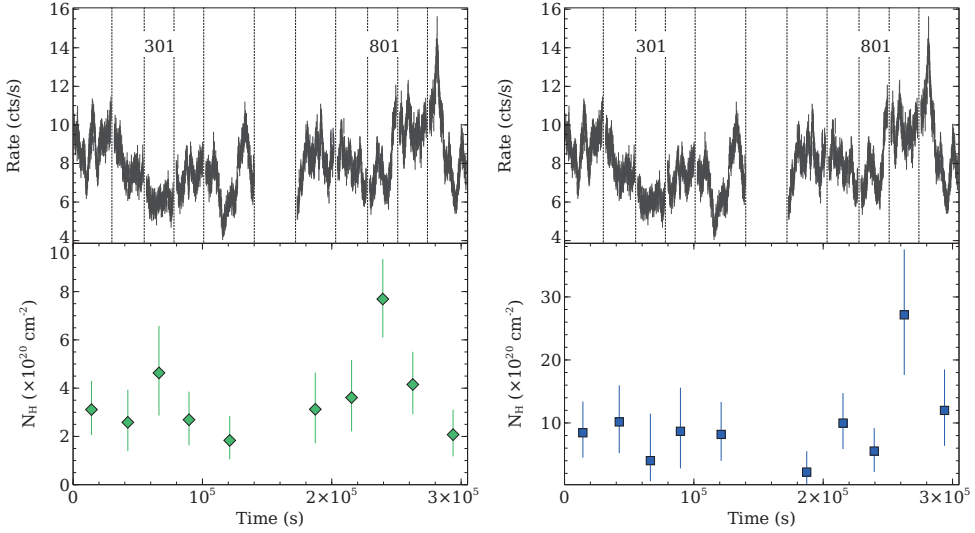


Figure 4.6: Best-fit parameters for the individual pointings. The behaviour of N_{H} with time (bottom panel) is shown for each one of the individual pointings (top panel). The ionization fixed of each of the gas components was fixed in these fits to the best-fit value we found while fitting the long segments.

Individual pointings

We fit, in the same manner as described above, the individual pointings to investigate possible variations on shorter timescales, and if such variability would directly relate to the intrinsic changes in the flux of the source. The best-fit parameters can be found in Table 4.6.

We firstly note that it is indeed difficult to constrain the warm absorber parameters for each of the individual pointings. The lower signal-to-noise ratio does not allow for reliable constraints on the ionization parameters of the two gas components. To enable us to constrain the changes in the column density more accurately, we have fixed the ionization state of each of the gas components to the best-fit value we found while fitting the long segments. As can be seen from Fig. 4.6 and Table 4.6, the column density of the two gas components does not appear to vary at a significant level (see lower panel of Fig. 4.6). However, the suggestive variations in the column density of component two during the second observation appear to roughly follow the flux changes in the source during this period. The highest value for the column density of component two is measured during the fourth pointing which encloses most of the flaring period. The flux during the fifth pointing first increases then undergoes an abrupt decrease. Due to the limits on the statistics it is not possible to split the fifth pointing and measure the column density for the high

Table 4.6: Best-fit parameters of the individual pointings. The count rate refers to the individual RGS spectra.

	$N_{\text{H, Comp 1}}$ ($\times 10^{20} \text{cm}^{-2}$)	$N_{\text{H, Comp 2}}$ ($\times 10^{20} \text{cm}^{-2}$)	Rate (cts/s)	C-stat/ <i>d.o.f.</i>
301-1	3 ± 1	8 ± 5	0.527 ± 0.004	1703/1540
301-2	3 ± 1	10 ± 5	0.468 ± 0.003	3217/2610
301-3	5 ± 2	4_{-3}^{+7}	0.358 ± 0.003	1773/1513
301-4	3 ± 1	9 ± 7	0.444 ± 0.003	1832/1612
301-5	2 ± 1	8 ± 5	0.445 ± 0.003	1988/1720
801-1	3 ± 1	2 ± 2	0.455 ± 0.003	3101/2646
801-2	3 ± 1	10 ± 5	0.455 ± 0.003	3165/2745
801-3	8 ± 2	6 ± 3	0.456 ± 0.003	1967/1708
801-4	4 ± 1	27 ± 10	0.578 ± 0.004	1889/1731
801-5	2 ± 1	12 ± 6	0.550 ± 0.004	1781/1648

and low-flux independently. Therefore we are not able to examine in more detail this suggestive correlation between the source's flux and the column density of the high-ionization component (see Fig. 4.7). Interestingly, in some cases, an apparent decrease in column density in component two corresponds to a potential increase in column density in component one, as seen for example between the second and third pointing of observation 801. When considering the two observations, however, the uncertainties do not allow to distinguish an anti-correlation in the behaviour of the column densities in both components (see Fig. 4.8).

4.4 Discussion

These new observations confirm the presence of two ionized absorbing gas components in the soft X-ray spectrum of I ZW 1. In this section we discuss our results in the light of previous observations and their implications in the context of warm absorber models and geometries.

4.4.1 A two component warm absorber

Our results are particularly interesting when placed in context with previous observations of I ZW 1 (See Table 4.7). I ZW 1 was firstly observed by XMM Newton in 2002 (see Gallo et al. 2004). When presenting the new soft X-ray data from 2005, Costantini et al. (2007a) characterized the warm absorber in both epochs by performing an analysis similar to this work, also using the XABS model available in SPEX. Costantini et al. (2007a) found that the soft X-ray spectra during both epochs required two warm absorber models, including low and high-ionization components, with similar column

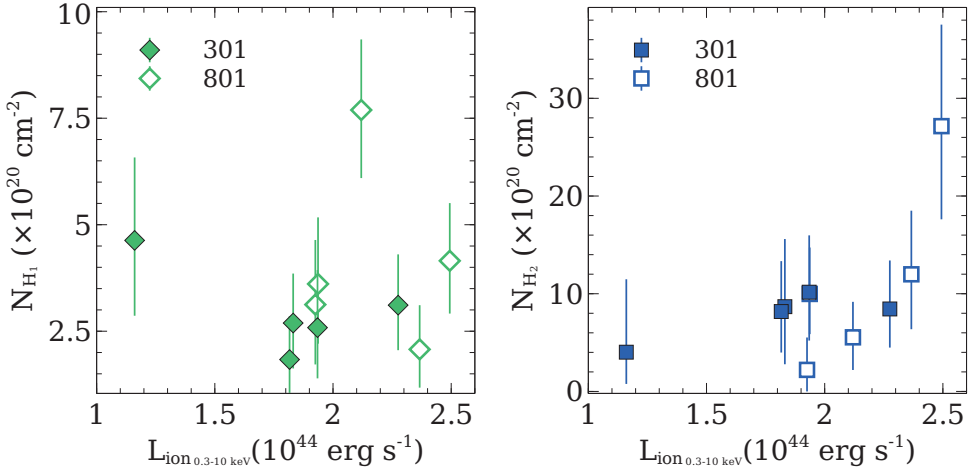


Figure 4.7: N_{H_1} (left) and N_{H_2} (right) plotted as a function of luminosity. The filled data points belong to the first observation, and the open data points belong to the second observation.

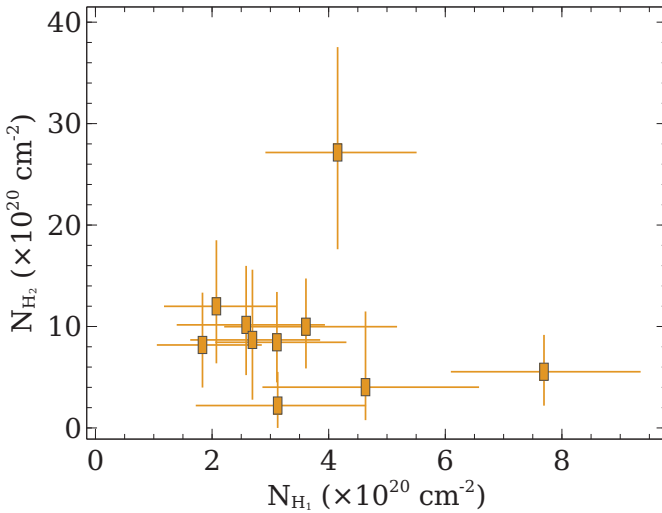


Figure 4.8: N_{H_2} plotted as a function of N_{H_1} . The variations in column density in component 2 do not appear to be correlated with variations in the column density of component 1.

Table 4.7: Recent history of the X-ray WA in IZW1

		N_{H} ($\times 10^{20} \text{cm}^{-2}$)	$\log \xi$	Velocity (kms^{-1})
Comp 1	2002	24 ± 5	-0.9 ± 0.2	-1800 ± 400
	2005	13 ± 3	0.05 ± 0.16	-1700 ± 400
	2015	3.4 ± 0.4	-0.23 ± 0.06	-1870 ± 70
Comp 2	2002	13 ± 4	1.6 ± 0.2	-
	2005	13 ± 5	2.6 ± 0.3	-
	2015	9 ± 2	1.96 ± 0.05	-2500 ± 100

densities. While the column densities did not change dramatically over those years, there was a variation of the ionization parameters of both components that oddly suggested an anti-correlation between the X-ray luminosity and the ionization state of both components of the gas. More interestingly, the low-ionization component was found to likely have a counterpart in the UV (see Laor et al. 1997; Costantini et al. 2007a). This component has been found to have the same outflow velocity since it was first observed in the UV (Laor et al. 1997). In Costantini et al. (2007a) an intrinsic neutral absorber was also identified. We find, in our analysis, that the improvement on the Galactic absorption measurements, which now include both the atomic and the molecular hydrogen components (Willingale et al. 2013), is likely be the reason why our fits do not require an extra neutral absorber. Furthermore, we do not identify an OI edge at the redshift of the source in these data, which would be present in the case of neutral absorption. Our observations show that the ionization state of the gas is lower for both components when compared to the last observations, even though the X-ray luminosity is higher in 2015 than it was in 2005 (see Table 4.7). Fig. 4.10 shows the X-ray luminosity in each of the epochs versus the estimated ionization parameter for each of the absorber components. The X-ray luminosity alone is a good diagnostic for ionizing luminosity in this case, since the X-ray ions are more sensitive to the X-ray photons rather than to the UV continuum (e.g. Netzer 1996). When photoionization occurs, a variable source will have an impact on the ionization balance of the gas. For an equilibrium situation, the gas responds instantaneously to such changes, becoming more ionized as the flux increases and recombining when the flux drops. In the presence of a low density gas (and depending on its distance to the continuum source), the response to changes in luminosity may be delayed which results in a complex time-dependent behaviour (Nicastro et al. 1999; Silva et al. 2016). Remarkably, I ZW 1 shows instead an apparent anti-correlation with X-ray luminosity on timescales of years. This could derive from a scenario in which the outflowing absorbing gas is in constant non-equilibrium with its ionizing source or, could result instead from the presence of transiting gas, crossing our line of sight.

In either case, the two warm absorber components must be linked. The two show

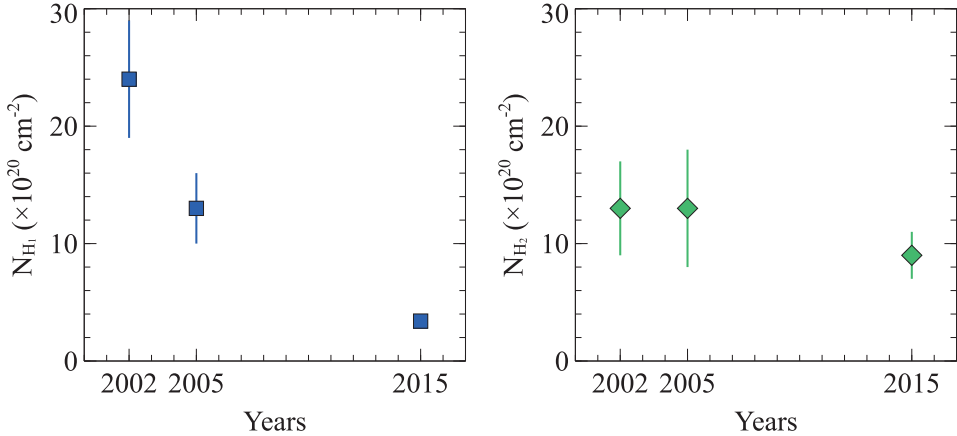


Figure 4.9: N_{H_1} and N_{H_2} behaviour throughout the years, for components 1 and 2 respectively. Please note that at this scale the error bars in the estimated value for the column density of component 1 in 2015 are within the size of the marker (see table 4.7).

the same ionization behaviour despite the X-ray luminosity and, although not formally consistent, the two also show very similar outflowing velocities. To co-exist, the two components are required to be in pressure equilibrium by classical warm absorber scenarios (see more in section 4.4.3). To investigate if the low and high-ionization phases of the absorbing gas are in pressure equilibrium, we have generated the thermal stability curves for I ZW 1 by plotting the pressure ionization parameter, Ξ as a function of the electron temperature, T , see Fig. 4.11. The pressure ionization parameter is defined as $\Xi = L/4\pi r^2 cp = \xi/4\pi ckT$, where c is the speed of light, p is the pressure, k is the constant of Boltzmann, and T is the electron temperature. We computed with CLOUDY the corresponding electron temperature for a grid of ionization parameters ξ , thus allowing us to estimate Ξ . The two ionized gas components are overplotted on the stability curves for each epoch. To be in pressure equilibrium both components would need to share the same Ξ . As it is clear from Fig. 4.11, this is not the case for the two gas phases, as they lie far apart in pressure ionization parameter. An alternative way to sustain the co-existence of both components which does not require pressure equilibrium is a scenario of radiation pressure confinement (Stern et al. 2014) or magnetic confinement (Rees 1987).

Furthermore, the column density of the low ionization component has dropped by at least a factor of three, since I ZW 1 was last observed in 2005 (see Fig. 4.9). Meanwhile, the outflow velocity of this component has remained constant for the past 20 years, when its UV counterpart was first observed.

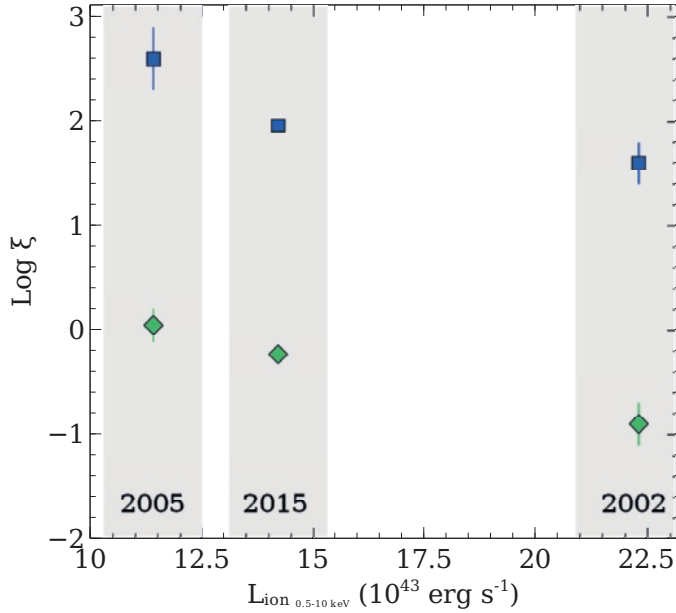


Figure 4.10: X-ray luminosity versus ionization parameter. The ionization state of both gas components do not correlate with the ionizing luminosity. Note also the similar behaviour of both gas components, suggesting the two gas phases may be linked. Notice that the ionization states of the gas is represented here over a broad range to accommodate both components. The changes in the ionization state of the gas throughout the years can be better appreciated in Table 4.7. Additionally, please note that at this scale the error bars in the estimated values for the column density of components 1 and 2 in 2015 are within the size of the marker (see table 4.7).

4.4.2 Short-time variability

The remarkable variability observed in the recent history of the warm absorber in I ZW 1 drove us to dissect these observations in different flux levels and timescales, in order to study the outflowing gas in more detail. In our analysis, we were not able to determine whether the ionization parameter of the gas changes despite the rapid variability in the intrinsic flux of the source. The column density of the gas, on the other hand, is potentially variable on such short timescales, particularly for component two.

During the second observation, the column density of component two, the high-ionization component, seems to vary on timescales of hours apparently following the intrinsic luminosity of the source. An increase in column density following an increase in luminosity is not a common occurrence in the study of warm absorbers. We stress that, since the column density increases with increasing luminosity, occultation phenomena can be excluded as an explanation for the potential short time variability

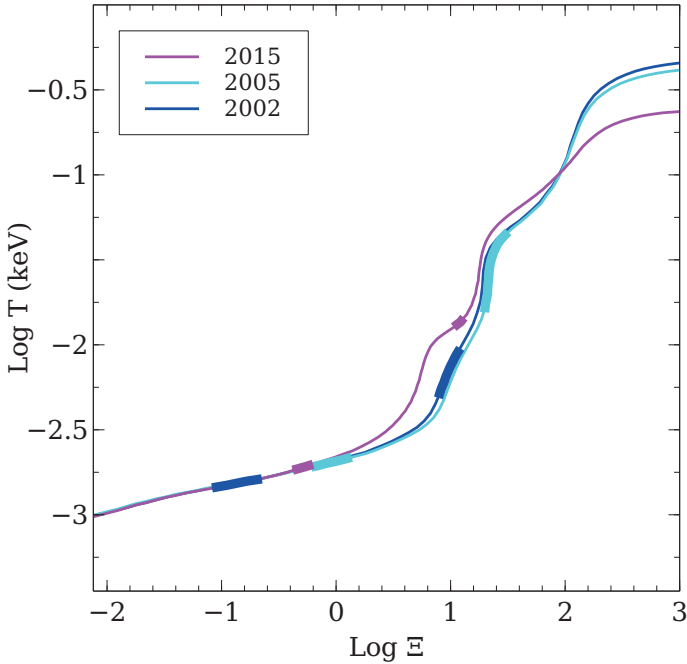


Figure 4.11: Stability curves for the different observations of I ZW 1 by XMM-Newton. The low and high-ionization warm absorber components are marked in the curves by the thicker lines.

in N_{H} . When presenting the timing properties of I ZW 1 during these observations, (Wilkins et al. 2017) has also found that the variability power in the coronal emission increases during the flare, which can be explained due an increase in the turbulence of the disc. For a disc driven flow, this could also induce variations in the warm absorber. Such apparent variations in our data, however, are not detected at a significant level.

4.4.3 The origin of the warm absorber in I ZW 1

Constraints on the location of the X-ray warm absorber are generally derived once the density of the gas is estimated. Estimating the density of the gas is only possible when the photoionized gas responds to changes in the ionizing continuum, allowing for a recombination timescale to be measured (see e.g. Krongold et al. 2007). In I ZW 1, instead of the expected linear response, we observe the ionization state of both gas components, while varying together, to be uncorrelated with the ionizing luminosity along the years and as such, photoionization equilibrium does not easily apply.

We can derive a crude estimate for the location of the warm absorber by assuming a spherical outflow with a uniform filling factor f , and a density that decreases with

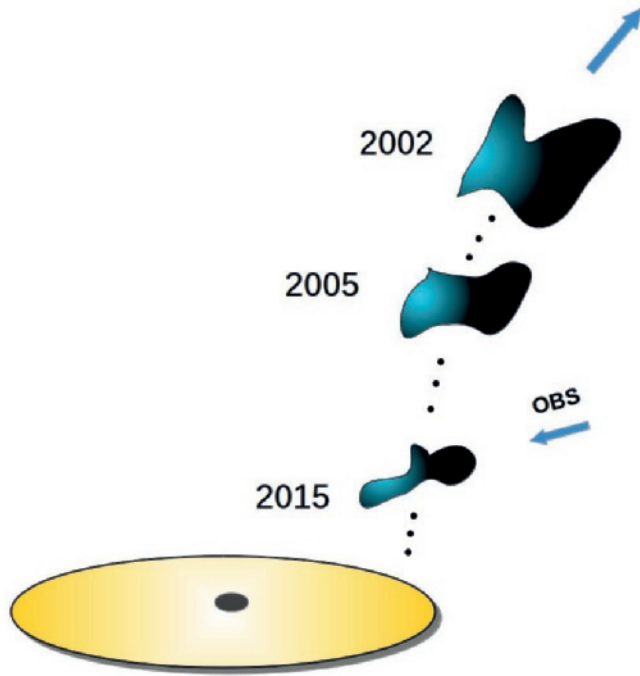


Figure 4.12: Schematic view of the phenomenological model for the warm absorber in I Zw 1. In this scheme, we highlight only the events we witnessed on the occasion of the observations with XMM-Newton throughout the years.

radius, $n(R)$. Following Blustin et al. (2005), we assume that all the warm absorber mass is contained within a thin layer of thickness Δr . The thickness of such a layer must be smaller than or at most equal to the distance of the warm absorber to the central source such that

$$\frac{\Delta r}{R} \leq 1. \quad (4.1)$$

The column density along our line of sight, for a specific ionization parameter ξ , can be expressed as a function of the gas density $n(R)$, the thickness of the layer Δr and the volume filling factor f as

$$N_{\text{H}} \sim n(R)\Delta r f. \quad (4.2)$$

Since the ionization parameter in the shell is given by

$$\xi = \frac{L_{\text{ion}}}{n(R)R^2}, \quad (4.3)$$

we get the maximum distance of the warm absorber to the central source

$$R \leq \frac{L_{\text{ion}} f}{\xi N_{\text{H}}}. \quad (4.4)$$

The volume filling factor f can be estimated by equating the momentum of the outflow to the momentum of the radiation it absorbs plus the momentum of the radiation it scatters (Blustin et al. 2005). Using the parameters from the best-fit of the averaged 2015 spectrum, we have calculate the volume filling factor in I ZW 1 to be $f_1 \sim 4 \times 10^{-5}$ and $f_2 \sim 3 \times 10^{-3}$, which respectively locates the warm absorber within 45 pc for component 1 and 9 pc for component 2.

A minimum radius for the location of the warm absorber can also be estimated by assuming the outflow velocity v_{out} is greater or equal to the escape velocity such that

$$R \geq \frac{2GM_{\text{BH}}}{v_{\text{out}}^2}. \quad (4.5)$$

This assumption would put the minimum location of the warm absorber at a distance of $R_1 \geq 0.07$ pc from the central source for component 1 and $R_2 \geq 0.04$ pc for component 2.

Understanding the variability of the warm absorber

In classical warm absorber models, the gas would be expected to respond to variations in the ionizing continuum. For thin spherical shells of material, the outflow is radially stratified, with the ionization of the gas being mostly dependent on its distance to the central source (see e.g. Steenbrugge et al. 2005). The long term variability observed on I ZW 1 suggests instead the density of the gas to be the main driver of the ionization. Alternatively, some studies have suggested a clumpy outflow in which tenuous hot, high-ionization, gas absorbs the X-rays, while surrounding discrete filaments of cold, low-ionization, UV absorbing gas. This scenario allows for the two components to be co-located and could explain the observed variability, but requires both phases to be in pressure equilibrium (Krolik & Kriss 2001). However, the high and low-ionization components observed in I ZW 1 are not in pressure equilibrium (see Fig. 4.11), and as such, this scenario also fails to be a candidate for the possible geometry of this outflow.

The peculiar characteristics observed for the warm absorber in I ZW 1 cannot be explained through classical warm absorber scenarios. To start with, changes in the ionization state of the gas throughout the years do not appear to be linked to variations in the ionizing luminosity as is expected for photoionization. Variations in the column density of the gas are also observed on long timescales. Furthermore,

these variations in ionization and opacity seem to be correlated for both components, which also happen to be outflowing at similar velocities. The outflow velocity of the low-ionization component, in particular, seems to be unchanged for the last 20 years, since its UV counterpart was first observed. We propose here an alternative geometrical model that could accommodate the apparent oddities of this source.

Due to the persistent outflow velocity observed in the colder component for the past two decades, we suggest that throughout all the observations of I ZW 1 we are observing of the same outflow event. The outflow is expected to be radiatively driven as the simultaneous UV data of this campaign seem to point out (Giustini et al. in prep.). In this picture, the gas identified in the UV/X-rays, the low-ionization component, primarily constitutes the flow. The skin layer facing the source would naturally become highly ionized, resulting in the observed high-ionization component which is detected only in the X-rays. This connection between the two components would offer a natural explanation for the similar kinematics ($v_{\text{Comp 1}} \sim -1900 \text{ km s}^{-1}$, $v_{\text{Comp 2}} \sim -2500 \text{ km s}^{-1}$), as well as for the correlated variability on long timescales regarding the ionization state and opacity of both gas components. This geometrical model we propose (see Fig. 4.12), considers the outflow to be clumpy. Different clumps, having different densities, and thus different ionization, cross the observer's line of sight at different epochs, resulting in the observed changes over the years, both in ionization and column density. In particular, the ionization state of the gas at different epochs is driven by different densities of the clumps and not by changes in the ionizing luminosity affecting gas components at different radii, as is usually assumed. This would explain the non-trivial behaviour of the ionization of the gas as a function of luminosity over long timescales. It is possible that the different clumps are individually in photoionization equilibrium with the ionizing luminosity. Also the changes in opacity for the different observations (2015, 2005 and 2002) can be easily understood as a natural consequence of a clumpy outflow.

The confinement of the warm absorber

As mentioned earlier in this paper, these observations were part of a multiwavelength campaign on this source, of which HST also took part. The UV data and its analysis will be further discussed in an upcoming paper (Giustini et al. in prep.), but its preliminary analysis has already shown 'line-locking', a signature of a radiatively driven wind, pointing to radiation pressure as the likely driving mechanism of the outflow (Proga et al. 2000). The driving radiation force can also compress the gas resulting in a scenario of radiation pressure confinement (Stern et al. 2014), which naturally explains a multiphase outflow without the need for pressure equilibrium between phases since the pressure increases significantly throughout the slab, with decreasing ionization. In a radiation pressure confinement scenario, the radiation pressure compresses the gas instead of accelerating it, which results in an outflow

with constant velocity, as observed in I ZW 1. Alternatively, magnetic confinement could also allow for a co-existence of the two warm absorber phases even if these are not in pressure equilibrium (Rees 1987).

4.5 Conclusions

We have performed a detailed analysis of the recent observations by RGS on board XMM-Newton of the narrow-line Seyfert 1 galaxy I ZW 1. The extensive modelling of the observed spectral features through time-averaged spectral fitting, flux resolved spectroscopy and time-resolved spectroscopy, we conclude the following:

1. We have confirmed the absorbing gas to be composed of two ionization phases, as previously reported by Costantini et al. (2007a) based on the historical data of I ZW 1. The long-lived low-ionization component ($\log \xi \sim 0$), which has been associated with the observed absorbing gas in the UV and whose outflow velocity has remained unchanged for nearly 20 years, and the high-ionization component ($\log \xi \sim 2$) have similar kinematic properties ($\sim -2000 \text{ km s}^{-1}$ and $\sim -2500 \text{ km s}^{-1}$ respectively). Furthermore, the long term variability of the gas suggests the two components to be linked.
2. The long-term variability of I ZW 1 disagrees with the commonly assumed scenario of photoionization equilibrium. The low and the high-ionization phases vary together in ionization state, yet these variations do not correlate with changes in the ionizing luminosity. This suggests the density of the gas to be the main driver of the observed changes in ionization, instead of a response to the variability of the ionizing source. The column density of the low-ionization component is also variable on timescales of years. The high-ionization component is consistent with being constant at such timescales. We have also studied the variability of the warm absorber on short-timescales. Our observations do not show significant variations on timescales of hours.
3. Classical warm absorber models fail to explain the complex variability of the ionized gas in I ZW 1. Instead, we propose a phenomenological model in which the gas originates from a inhomogeneous clumpy outflow, possibly radiatively driven. The low-ionization component primarily constitutes the flow, while the skin layer of the clumps facing the ionizing source becomes more ionized and accounts for the high-ionization phase observed. In this scenario, the ionization of the gas is primarily dependent on the density of the clumps. Different clumps have different densities, hence the observed variability in ionization throughout the years. Our estimates suggest the gas to be located between 0.07 pc and 9 pc, implying that the outflow may even be originating from the accretion disc.

The non-typical behaviour of the warm absorber in I ZW 1 demonstrates that, despite extensive studies, these systems are still not fully understood and substantiates the need for new theoretical models capable of reproducing such complex behaviour, particularly regarding the variability of the gas. Furthermore, long and, in particular, multi-wavelength observations are crucial to fully characterize the warm absorber zoo in AGN and assess the potential impact of the ionized gas to AGN feedback.